INORGANIC CHEMISTRY
FRONTIERS

RESEARCH ARTICLE

View Article Online
View Journal

Cite this: DOI: 10.1039/d6qi00665e

Dynamic covalent switching between a 1,1′-ruthenocene macrocycle and a ruthenocenophane through a transimination reaction

Max Roemer, *[a] Gilles Frison [b] and Han Vinh Huynh *[a]

Received 1st April 2026,
Accepted 25th April 2026

DOI: 10.1039/d6qi00665e

rsc.li/frontiers-inorganic

Dynamic covalent chemistry has been employed extensively for connecting amine and aldehyde building blocks to construct organic macrocycles, covalent organic frameworks, and organometallic analogues. However, detailed investigations on covalent dynamic imine chemistry involving metallocenes and diamines are sparse. The synthesis of a 1,1′-ruthenocene-diimine macrocycle (**2a**) by a condensation reaction of 1,1′-diformylruthenocene (**1**) and 1,4-diaminobutane is described. The reaction is high-yielding in solution and under mechanochemical conditions. A dynamic equilibrium between dinuclear **2a** and mononuclear ruthenocenophane (**2b**) was discovered, which allows the synthesis of ruthenocenophanes through dynamic covalent chemistry and further modification. Compounds **2a** and **2b** can be interconverted in solution by adjusting the temperature or concentration. Reactive **2b** can be trapped by reactions at the imine functions, as a diiminium cation through a reaction with an acid, and as a trimetallic adduct **3b**, through reaction with a palladium N-heterocyclic carbene (NHC) complex. Similarly, a stable hexametallic macrocycle **3a** was isolated by reaction of **2a** with the palladium NHC complex. The transformation between **2a** and **2b** proceeds by dynamic transimination. The reactions are likely water-catalysed with several intertwined pathways, and the self-sorting system can be kinetically controlled. A mechanism supported by control experiments and density functional theory calculations is proposed.

Introduction

Gaining control of one molecular state over another in a switchable system is crucial for regulating molecular properties in physical chemistry, synthetic chemistry, and surface science. Switching has been employed in catalysis to toggle the outcome of a chemical reaction,[1] in molecular electronics to modulate electrical currents on the nanoscale,[2–4] and in molecular recognition to turn host–guest interactions on or off.[5,6] Dynamic covalent chemistry (DCC) is a well-established approach for connecting building blocks equipped with amine and aldehyde functional groups, which condense to imines, affording larger scaffolds such as macrocycles. Upon imine formation, one equivalent of water is generated, and the reaction is reversible as the imine may hydrolyse under regeneration of aldehydes and amines, which constitutes a dynamic equilibrium. This has been investigated extensively and may be used to enable chemical switching between different states. As such, DCC forms the basis of many impressive transformations and syntheses of various structural motifs. These include molecular walkers, molecular motors, interlocked cyclic structures, and covalent organic frameworks (COFs).[7,8] Furthermore, it has been employed in self-sorting systems containing molecules with different grades of functionalization.[9–12] Ferrocene-based macrocycles have also been prepared by DCC, yielding COFs containing organometallics.[13,14] Controlled switching of these systems has not been realised, and similar ruthenocene analogues are yet to be prepared and investigated. Metallocenophanes are organometallic analogues of cyclophanes, in which both Cp-ligands of a sandwich complex are connected *via* a bridge.[15] This bridge can induce a ring strain, which may be of advantage for ring-opening polymerisations. In 1,1′-fused dinuclear metallocenes, one complex bridges the other, and these systems constitute macrocycles. The reversible switching of nickelocenophanes into polymers has been reported for labile carbon-bridged nickelocenes *via* ring-opening polymerisation.[16–18] Different carbon-bridged metallocenophanes have been reported, including derivatives with unsaturated bridges,[19,20] nitrogen functions,[21–24] and fluorinated bridges.[25] Among the reported metallocene-based macrocycles,

[a]*Department of Chemistry, National University of Singapore, 3 Science Drive 3, Singapore 117543. E-mail: max.roemer@nus.edu.sg, chmhhv@nus.edu.sg*
[b]*Sorbonne Université, CNRS, Laboratoire de Chimie Théorique, 75005 Paris, France*

ferrocene in combination with organic building blocks has been employed most frequently.[26–28] Less studied, as significantly more challenging to obtain, are oligomeric rings of 1,1′-interconnected ferrocenes.[29] Some macrocyclic ruthenocene-derived compounds have been reported, including sulfur- and oxygen-containing *ansa*-type cycles,[30] aza-crown ether derivatives with ruthenocene in a side chain,[31] and different porphyrin derivatives with ruthenocenes incorporated.[32] Different macrocyclic ferrocene 1,1′-diimines have been prepared, reduced to amines, and employed in anion recognition.[33,34] In contrast, only very few ruthenocene-based alkyl imines have been reported. The known derivatives include a ruthenocene–methylimine[35] and some polynuclear ruthenocenes,[36] including a macrocycle containing two ruthenocene units connected by conjugated imine–alkene bridges.[37]

Herein, we report on a ruthenocene–diimine macrocycle (**2a**) synthesised by dynamic covalent imine chemistry between 1,1′-diformylruthenocene (**1**) and 1,4-diaminobutane (DAB). The macrocycle may be thermally converted to a ruthenocenophane (**2b**). Both **2a** and **2b** are in a temperature- and concentration-dependent dynamic equilibrium in solution, and **2a** can be converted to **2b** by heating. The transformation is reversible as **2a** is regenerated upon cooling, and the mixture can be switched multiple times without loss of activity.

Results and discussion

Synthesis of the ruthenocene–diimine macrocycle

Condensation of **1** with terminal diamines can potentially lead to the formation of a mononuclear ruthenocenophane, a dinuclear 1,1′-ruthenocene–diimine macrocycle, oligonuclear metallomacrocycles, or polymers through a polycondensation reaction. We first assessed the reaction of **1** with an excess of DAB in solution (Scheme 1a) and isolated the macrocycle **2a** in good yield after recrystallisation. A ferrocene-based analogue of **2a** has been reported previously.[33] Inspired by a recent report on the mechanochemical formation of imine cages involving 1,1′-diformylferrocene,[13] we tested the mechanochemical synthesis of **2a** by grinding **1** with DAB (Scheme 1b). Indeed, **2a** forms in a quantitative yield through a solvent-free reaction in 30 minutes by simply grinding both reactants with a glass rod. Imine-based Cu and Fe complexes were reported to form by ball milling of organic aldehydes and amines in the presence of metal salts, speeding up conventional solution synthesis significantly.[38] Single crystals of **2a**, **2a**·DCM, and **2a**·H_2O suitable for X-ray diffraction were obtained. The molecular structure of **2a**·DCM is shown in Scheme 1c (Fig. S1 and S2). Attempted analysis of **2a** by ^{1}H and ^{13}C NMR spectroscopy always revealed minor amounts of another species, which has been assigned to **2b**. For a clear distinction, **2a** is referred to as "macrocycle" and **2b** as "ruthenocenophane" henceforth. Furthermore, the composition of the mixture in the solution changed upon standing, showing an increase in **2b** with time.

Due to symmetry, both compounds exhibit simple ^{1}H NMR spectra showing the same coupling pattern, but with different chemical shifts: one singlet for the imine protons at 7.86 ppm (**2a**) and 7.78 ppm (**2b**), two pseudo triplets for the Cp-protons, and the resonances for two distinct methylene units. Detailed 2D NMR experiments (COSY, HSQC, HMBC and DOSY Fig. S3–S13) were conducted on the mixture, which allows a distinction between both components and assignment of the resonances.

Dynamic equilibrium

We then monitored a solution of **2a** in chloroform-*d* upon heating in an NMR tube, by simultaneously recording NMR spectra at fixed intervals. This experiment confirmed a transformation from **2a** to **2b** (Scheme 2).

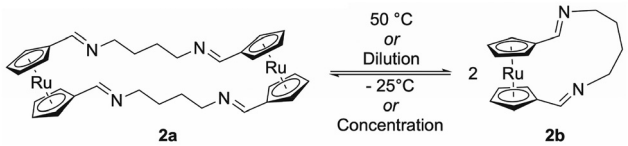

Scheme 2 Solution-state dynamic equilibrium between the macrocycle **2a** and the ruthenocenophane **2b** observed by NMR spectroscopy in chloroform-*d*.

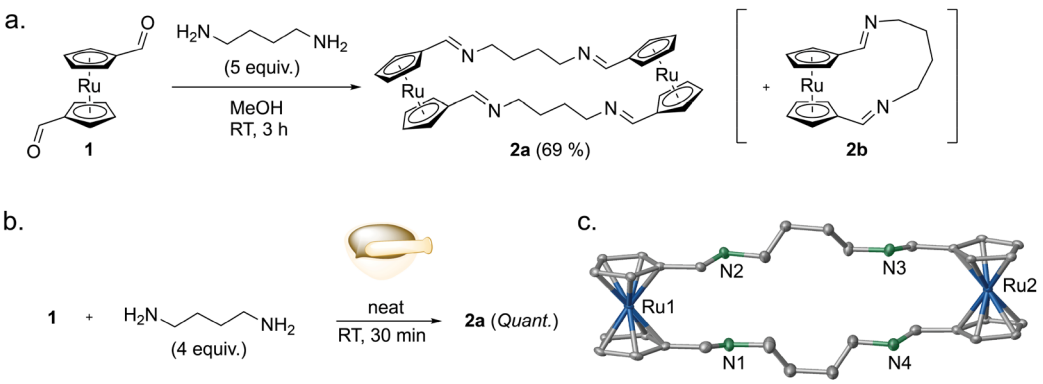

Scheme 1 (a) Synthesis of the macrocycle **2a** from **1** and 1,4-diaminobutane in solution. (b) Mechanochemical synthesis of **2a**. (c) Molecular structure of the macrocycle **2a**·DCM, obtained by single crystal X-ray diffraction. H-atoms and a dichloromethane solvate molecule have been omitted for clarity.

Upon heating the sample to 50 °C, 40 ^{1}H NMR spectra were recorded at a fixed interval of two minutes. Immediately, the resonances of **2a** began to decline, while the resonances of **2b** gained intensity. Fig. 1a shows overlays of the ^{1}H NMR spectra of a freshly prepared sample of **2a** in chloroform-*d* at room temperature and selected spectra recorded at different time points after heating and after cooling the sample. The remaining NMR spectra are shown in the SI (Fig. S16). The relative ratios of the two species at the different time points were determined by comparing the integrals of their iminic ^{1}H NMR resonances (Fig. 1a and b). After approximately 30 minutes of heating, the switching stalled, and the mixture reached a steady state with >70% **2b**.

We further performed ^{1}H DOSY (diffusion ordered spectroscopy) NMR measurements before and after heating the sample, confirming that the smaller species (**2b**) formed during the transformation indeed diffuses faster than the larger species (**2a**). Both species are clearly separated in DOSY, allowing assignment of the ^{1}H NMR resonances of each component in the mixture (SI, Fig. S11 and S13). We then assessed the influence of residual water on the reaction outcome. Initially, the transformation was conducted in chloroform-*d* treated with K_2CO_3 (blue and green traces, Fig. 1b). Next, chloroform-*d* dried by distillation from CaH_2 was tested to evaluate whether this slows the transformation, as it contains less water. However, we observed the opposite: the transformation accelerated (Fig. 1b, black and red traces). This was puzzling and, at first glance, suggested that the reaction is not water-catalysed. For the ferrocene-based analogue, no such transformation to a ferrocenophane was reported.[33] However, several ferrocenophane-based systems were reported to form from reactions of 1,1′-diformylferrocene with tri- and polyamines.[34,39] In some cases, ferrocenophanes formed preferentially during synthesis. Others have argued that the differences are mainly due to the lengths of the diamines: shorter diamines form macrocycles, while longer ones form ferrocenophanes.[34] In none of these cases was any spontaneous transformation to other species in solution mentioned. This is perhaps because in many examples, the imines were directly reduced to amines, thus locking this function for further DCC.

Metallocenophanes were previously prepared by the cyclisation of 1,1′-unsaturated carbon chains, and various mechanisms have been proposed. These include ring formations *via* nucleophilic addition,[20,40] redox-autocatalysis,[25,41] and cascade cyclisations.[21,22] Here, we discovered a novel approach in which handle formation is entropy-driven and can be

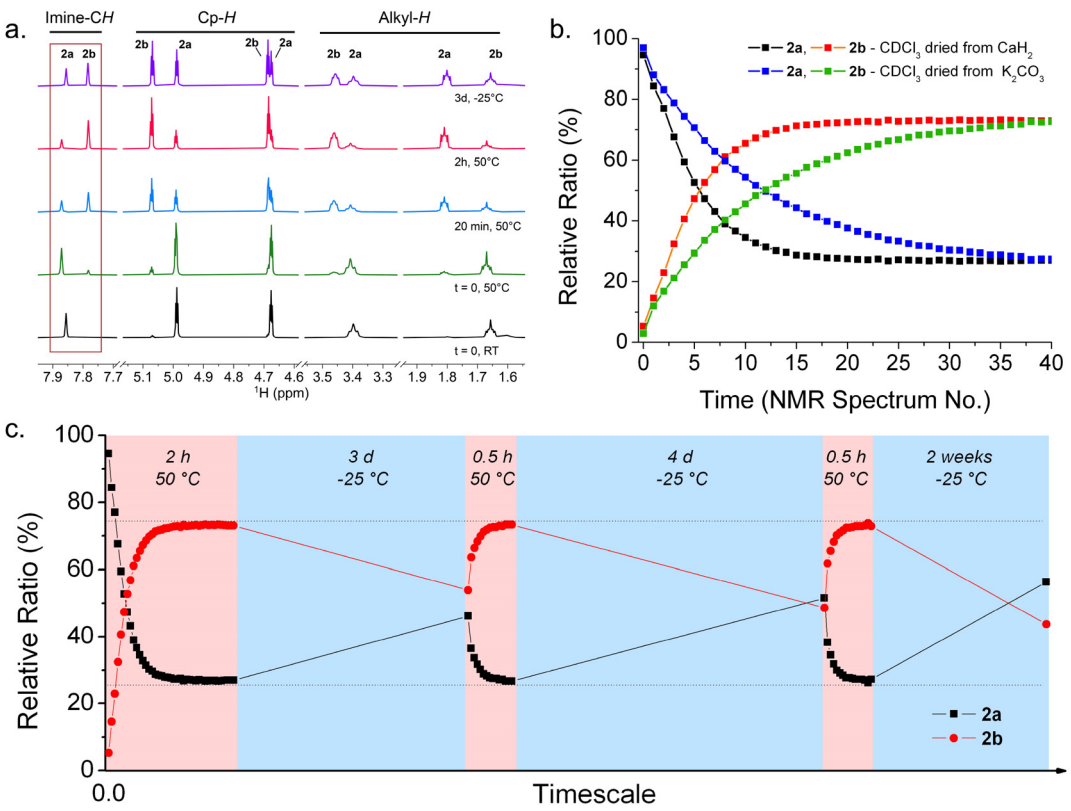

Fig. 1 Switching cycles of the dynamic equilibrium between **2a** and **2b**. (a) ^{1}H NMR spectra in chloroform-*d* of the mixture at different time points of a switching cycle. The resonances of **2a**/**2b** shift subtly at 50 °C relative to room temperature (RT). The region of imine resonances used to determine the **2a**/**2b** ratio is indicated by the box. (b) Overlays of the first conversion of **2a** to **2b** in chloroform-*d*, indicating a faster conversion in CaH_2-dried chloroform-*d*. The red and black traces were constructed from the same data as illustrated in (a). (c) The black (**2a**) and red (**2b**) traces represent the relative amounts of the compounds. The lines serve as a guide for the eye only. A red background denotes conversions from **2a** to **2b** and a blue background denotes the reverse reaction. These regions are not to scale with each other.

achieved through DCC. Interestingly, upon cooling the sample to −25 °C, the mixture equilibrated back under regeneration of **2a**. This reverse reaction is significantly slower and results in an approximate 1 : 1 ratio of **2a**/**2b** upon standing for several days (Fig. 1c). Next, the sample was subjected to another heating cycle (15 spectra, 40 minutes in total), and the system switched again to **2b** without any loss of activity. After successfully switching the system, we conducted several such cycles, and no loss of activity was observed (SI, Fig. S16–S18). Standing for over two weeks yielded only a slightly higher ratio of **2b** *vs.* **2a** than standing for a few days. Fig. 1c shows the relative product ratios after repeated switching cycles in CaH_2-dried chloroform-*d*. For comparison, several such switching cycles were conducted in K_2CO_3-treated chloroform-*d* as well (SI, Fig. S20–S24). We tested switching fatigue by running one forward–backward sequence in the presence of 1,3,5-trimethoxybenzene as an internal standard, which confirmed a steady integration of ^{1}H NMR resonances of the internal standard *vs.* imines. In the absence of any significant amounts of side-products, this indicates a robust system. Consistent for all the cycles, the transformation was faster in CaH_2-dried than in K_2CO_3-treated chloroform-*d*. While the presence of **2b** could be confirmed by NMR spectroscopy and high-resolution mass spectrometry, isolating the species proved challenging, so further experiments were conducted. Preparation of **2b** by heating a solution of **2a** in chloroform-*d*, followed by concentration, always resulted in a back-conversion to **2a**. Furthermore, the macrocycle **2a** is significantly larger and has a lower solubility in common organic solvents, which led to its preferred crystallisation. The initial switching experiments were conducted at a concentration of 4.4 mM in chloroform-*d*, and the maximum **2b** content after heating was <75%. Lowering the concentration to 1.5 mM resulted in a higher **2b** content of 86% after heating. However, upon concentration, the mixture still reverted to **2a**.

Trapping experiments

Since the isolation of **2b** was not possible, attempts were made at trapping it with electrophiles. Imines readily react with Lewis acids, and the resulting acid–base adducts are expected to halt the reverse reaction to **2a**. Thus, **2a** was switched to **2b** by refluxing it in chloroform, followed by the addition of HCl in ether. Indeed, the diiminium cation $[H_2\text{-}\mathbf{2b}]^{2+}$ easily formed, which could be isolated in different forms (Scheme 3).

Initially, we directly crystallised $[H_2\text{-}\mathbf{2b}]^{2+}$ from the reaction mixture by slow liquid diffusion of pentane into a chloroform-*d* solution. This yielded single crystals, which were very sensitive once removed from the solution. On exposure to air, they became instantly brittle and decomposed within seconds. Single crystal X-ray diffraction confirmed the presence of the doubly protonated ruthenocenophane $[H_2\text{-}\mathbf{2b}]^{2+}$ (Fig. 2a). Notably, it contained three Cl^- counterions in combination with a further $H_5O_2^+$ cation, which is known as the Zundel cation.

The atomic positions of the iminium protons and the protons of the Zundel cation were obtained from the diffraction map. Important bond lengths and angles are reported in Table S3 (SI, page S33). Zundel cations are interesting and relatively rare species, first described by Zundel in 1968.[42] Together with hydronium cations (H_3O^+) and Eigen cations ($[H_3O(H_2O)_3]^+$), they form the basis of various investigations of hydrated protons. The ions have been studied in solution by X-ray absorption spectroscopy[43] on metal surfaces by scanning tunnelling microscopy[44] and in the solid state by crystallography.[45–49] For example, the Zundel cation was previously crystallised with nitranilic acid,[46,47] hydrated 1,8-bis(dimethylamino)-naphthalene hydrochlorides,[49] and protonated *N*,*N*,*N*,*N*-*peri*(dimethylamino)naphthalene chloride.[48] In chloride-containing systems, it is stabilised by chloride ions, forming infinite chains in the crystal. Like these organic precedents, the Zundel cation in the current organometallic system is stabilised by H-bonding to four chlorides. We have further discussed the crystallographic data, including Hirshfeld analysis, in the SI (pages S31–S38).

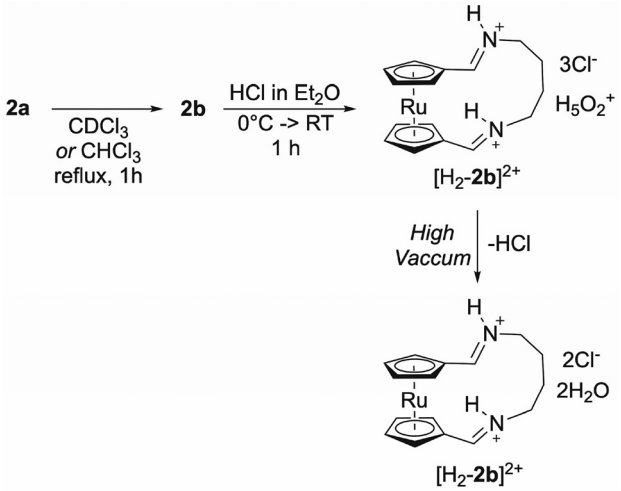

Scheme 3 Trapping of **2b** as the dication $[H_2\text{-}\mathbf{2b}]_2^+$, co-crystallised with a Zundel cation $[H_2\text{-}\mathbf{2b}]Cl_2{\cdot}(H_5O_2)Cl$ and the removal of HCl to yield $[H_2\text{-}\mathbf{2b}]Cl_2{\cdot}2H_2O$.

The formation of the Zundel cation arises from the excess HCl used in the reaction and residual water. We cannot fully exclude water residues from the starting material, and the commercial HCl solution in diethyl ether likely contains them as well. Compound **2a** can also crystallise with water molecules in the cavities (SI, Fig. S2), showing that the hydrated macrocycle is stable in the presence of water. This water can be trapped in the crystal lattice, likely making it difficult to remove by drying in a vacuum. In contrast, it is expected that HCl removal can be facilitated by applying a high vacuum. Thus, we subjected the crude reaction mixture to vacuum drying, which indeed removed the excess HCl and allowed crystallisation of $[H_2\text{-}\mathbf{2b}]Cl_2{\cdot}2H_2O$ without the Zundel cation. Two different types of crystals formed, and both the blocks ($C2/c$) and needles ($P2_1/n$) contained the dication $[H_2\text{-}\mathbf{2b}]^{2+}$, which co-crystallised with two water molecules and two chlorides. Their molecular structures are shown in Fig. 2b and c.

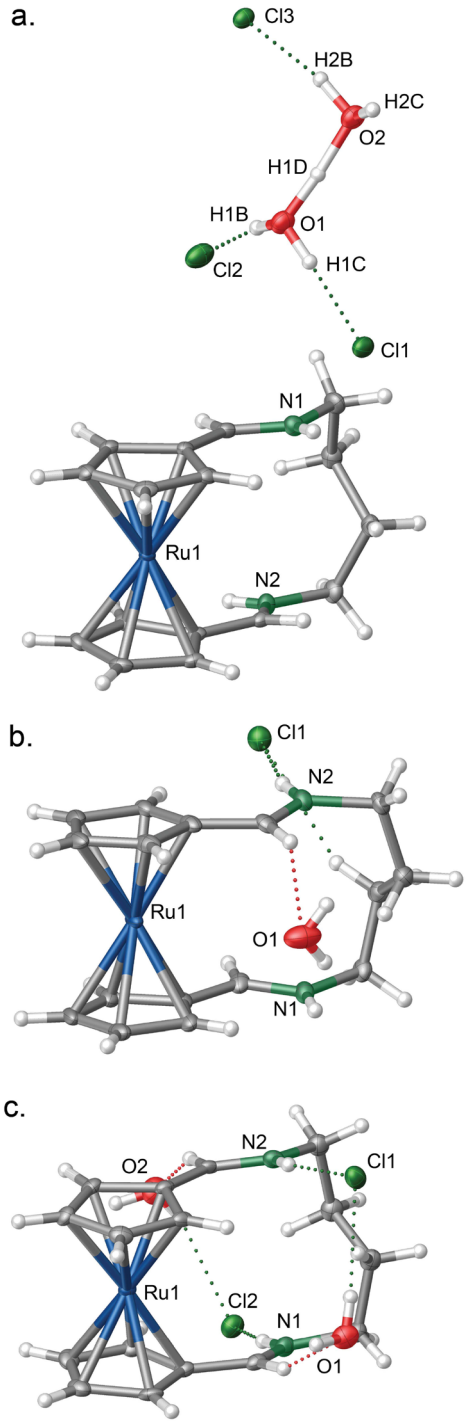

Fig. 2 Molecular structures of $[H_2\text{-}\mathbf{2b}]Cl_2{\cdot}(H_5O_2)Cl$ containing a Zundel cation stabilised by three chlorides (a) and the two different modifications of $[H_2\text{-}\mathbf{2b}]Cl_2{\cdot}2H_2O$: (b) *C*2/*c* and (c) $P2_1/n$.

Notably, in the $P2_1/n$ space group, a cage-like structure was obtained (SI, Fig. S32). The sensitive $[H_2\text{-}\mathbf{2b}]^{2+}$ decomposed upon exposure to air but remained stable under an argon atmosphere.

We further assessed the coordination chemistry of **2a** and **2b** with a palladium N-heterocyclic carbene (NHC) complex fragment (Scheme 4). For this, a well-established procedure was followed by cleaving the dimeric $[PdBr_2(^iPr_2\text{-bimy})]_2$ complex ($^iPr_2$-bimy = 1,3-diisopropylbenzimidazolin-2-ylidene) with **2a**/**b** in acetonitrile.[50,51] Compound **2a** was used without conversion to **2b**, although the reaction mixture was heated gently to increase the solubility of the starting material. The hexametallic ruthenocene macrocycle **3a** was obtained as the major product in 56% yield. It was sparingly soluble in acetonitrile and precipitated from the reaction mixture upon cooling, which allowed easy isolation by filtration. The filtrate was further concentrated, yielding single crystals of the trimetallic ruthenocenophane **3b**. Compound **3b** was only characterised by single crystal X-ray diffraction and high-resolution mass spectrometry. The molecular structures of the multimetallic complexes are shown in Fig. 3. The ring system of the macrocycle of **3a** was expanded in a wider manner compared to **2a**, as the imine substituents of the ruthenocenes were situated in a 1,2′-conformation to accommodate the four Pd-NHC units.

Compound **3a** crystallised with half a molecule in the asymmetric unit, and the intramolecular Pd–Pd distance is 6.7265(7) Å, which is unobstructed with no other atoms in between. In **3b**, the Pd-NHC units point away from each other with a larger Pd–Pd distance of 7.3992(6) Å due to the separation by the ruthenocenophane handle. The important bond lengths are summarised in Table S5 (SI, page S38). The Pd–C bonds in **3a** and **3b** range from 1.959(3) to 1.974(3) Å, compared to 1.947(3) Å for the starting material $[PdBr_2(^iPr_2\text{-bimy})]_2$[50] and 1.953(4) Å for a reported (mononuclear) pyridine analogue.[52] The slightly longer bond is due to a stronger σ-donating ability, as evinced by the determination of its Huynh electronic parameter (HEP).[51] The HEP value obtained from **3a** was 163.7 ppm, compared to 159.5 ppm for pyridine.[52] The very small amounts of **3b** available precluded the determination of its HEP value.

Mechanism of the dynamic transimination

Having gained reasonable control over the dynamic equilibrium, we investigated the mechanistic aspects of the macrocycle to ruthenocenophane transformation. Such transformations are known to be driven by entropy,[8] as at elevated temperatures, the presence of more, smaller molecules, relative to fewer, larger molecules, is favoured. The reverse applies when cooling the mixture. Similar effects apply when diluting a solution: the dilution pushes the equilibrium towards more molecules, whereas a more concentrated solution behaves in the opposite way. From a mechanistic perspective, the most likely pathway for the transformation appears to be water-catalysed, as imine–amine equilibria are well known. Imine–amine[53] and imine–imine scrambling have been reported,[54] and are referred to as transimination and imine metathesis, respectively. A control experiment was conducted by adding an excess of an alkylamine to **2a** and heating the mixture in chloroform-*d* (Scheme 5a). This led to the formation of scrambling products that were evident in the resulting ^{1}H NMR spectrum (SI, Fig. S27 and 28). Mass spectrometry confirmed the presence of **2c** and **2d**, showing that macrocycle **2a** opens upon reaction

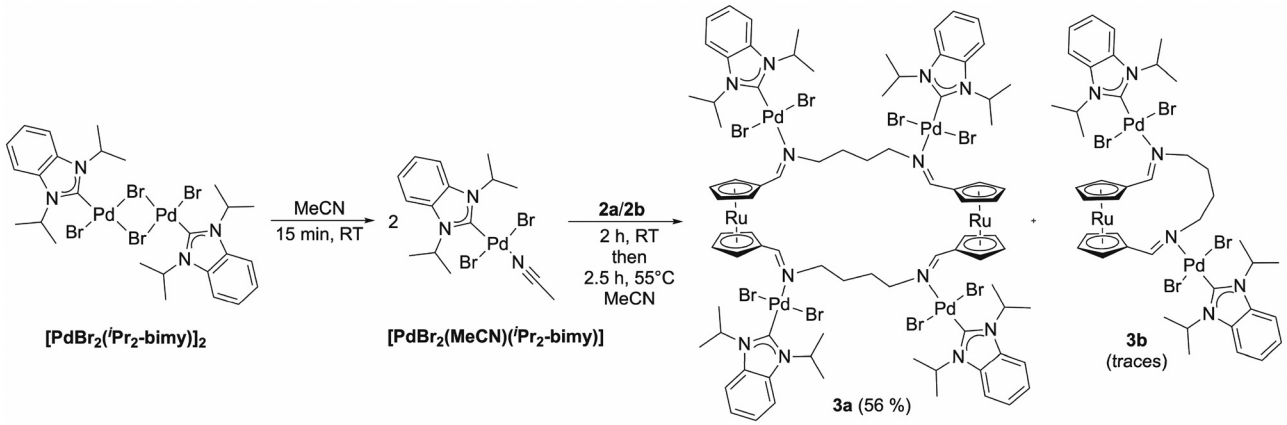

Scheme 4 Synthesis of the hexametallic macrocycle **3a** and the trimetallic ruthenocenophane **3b** by a reaction of [$PdBr_2$(MeCN)(^{i}Pr_2-bimy)] with **2a** and **2b**.

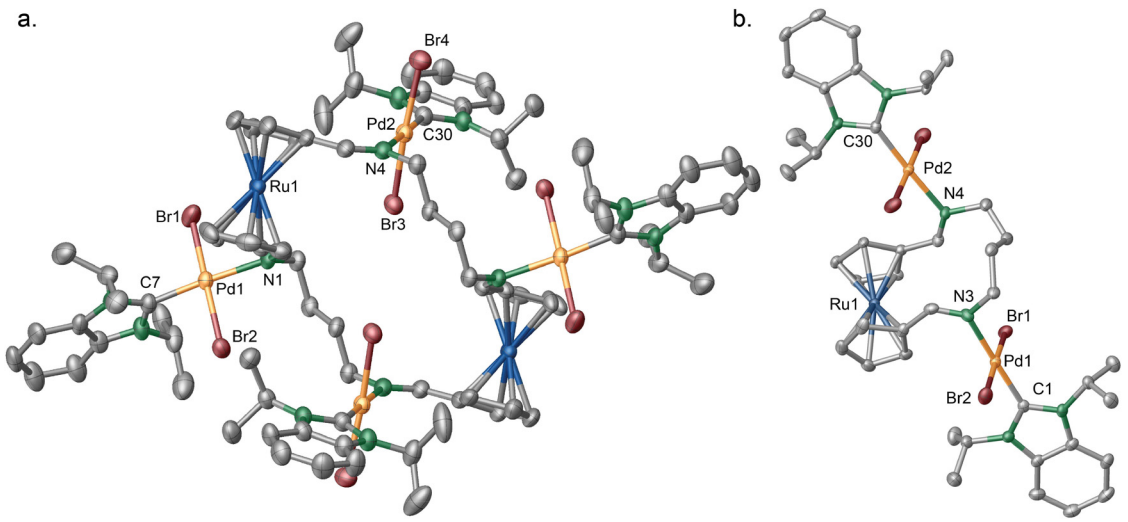

Fig. 3 Molecular structures of the hexametallic macrocycle **3a** (a) and the trimetallic ruthenocenophane **3b** (b), determined by single crystal X-ray diffraction. Acetonitrile solvate molecules, H-atoms, and a disorder in the [8]-handle of **3b** were omitted for clarity.

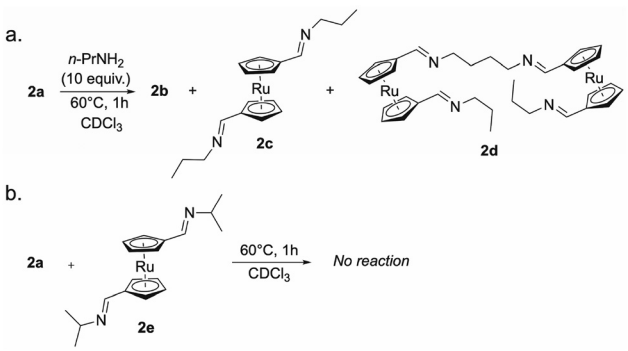

Scheme 5 Control experiments. (a) Reaction of **2a** with an excess of *n*-propylamine under typical conditions for the transformation of **2a** to **2b**. (b) Attempted reaction of **2a** with a stoichiometric amount of the ruthenocene–diimine **2e**.

with a free amine. Subsequently, a reaction with a free 1,1′-ruthenocene-diimine (**2e**) was assessed. For this, we mixed **2e** with **2a** in a 1 : 1 ratio under typical conditions for the transformation of **2a** to **2b**. No imine scrambling occurred, and thus, imine metathesis can be ruled out. Interestingly, the transformation of **2a** to **2b** was also inhibited, and the reaction mixture contained traces of free isopropylamine observed by ^{1}H NMR spectroscopy. This suggests that **2e** acted as a water trap. It is likely that any residual water in the mixture reacts preferentially with **2e**, the smaller and presumably more reactive molecule. We further tested the transformation in the presence of bulk 4 Å molecular sieves as water-absorbing agents. This, however, led to most of **2a** being eliminated from the solution, presumably through interaction with the molecular sieves. Based on these observations and the likely involvement of multiple bifunctional reactive species, we propose the mechanism shown in Scheme 6. On the way from **2a** to **2b**,

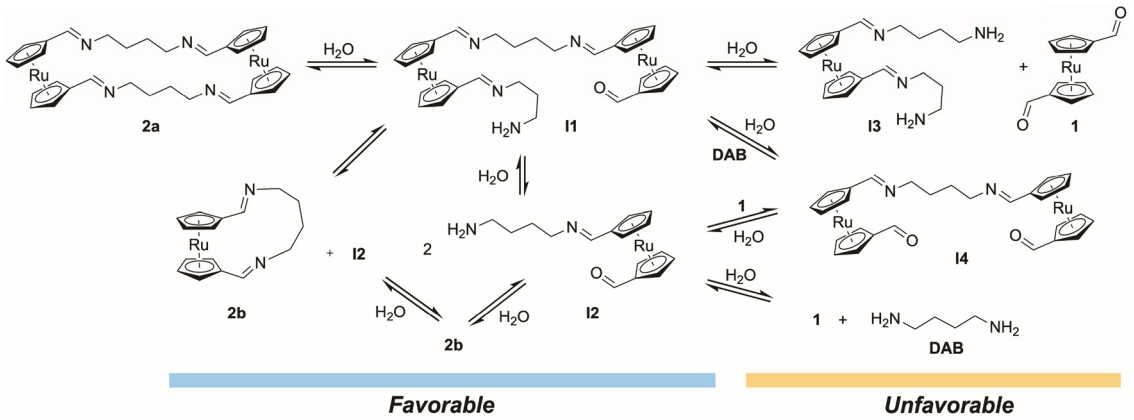

Scheme 6 Plausible pathways for the reversible transformation of **2a** to **2b**. The key intermediate is **I1**, which may cyclize directly to **2b** by intramolecular transimination and *via* **I2**. Other hydrolysis steps resulting in the formation of **I3**, **I4**, **1** and DAB are unfavourable and slow down the transformation.

compound **2a** likely opens by hydrolysis to give **I1** as the key intermediate. **I1** can further hydrolyse to produce two equivalents of intermediate **I2**, one equivalent each of **I3** and **1**, **I4** and **1**, and DAB. And **I1** may close again by intramolecular condensation to **2a**. **I2** can react back to **I1** through combination with another equivalent of **I2** to give **I1**. Furthermore, **I1** may react directly to **2b** by an intramolecular transimination, which in turn generates another equivalent of **I2**. The direct transimination of **I1** to **2b** is the pathway requiring the fewest steps, but it requires water to initiate the transformation. All hydrolysis steps to **I2**, **I3**, **I4**, **1**, and DAB require more water, and are unfavourable for the formation of **2b**, which could explain the experimental observation of a slower transformation with chloroform-*d* dried over K_2CO_3 than with CaH_2, as the former retains more residual water. For example, the formation of **I3** from **I1** generates one equivalent of **1**. Since **1** contains two aldehyde functions, it would require reactions at both functions with a free amine to ultimately regenerate **2b**. Similarly, the route from **I4** to **2b**, *via* **I2**, requires an additional step of forming **I2**. The magnified baselines of the VT NMR spectra for switching in chloroform-*d*, distilled from CaH_2 (SI, Fig. S19, last cycle), do not show evidence of aldehyde signals. In contrast, the switching in chloroform-*d*, dried over K_2CO_3, shows a low-intensity signal at 9.7 ppm, visible after spectrum number 20 (Fig. S25). The signal evolves slightly across the different cycles, but the overall intensity remains low (<1%) relative to the total imine resonances in the last run (Fig. S26). This signal matches the chemical shift of **1**[55] and likely originates from the involved aldehyde functional groups of **1** and/or the intermediates **I1**/**I2**/**I4**. Its absence in the dryer chloroform-*d* further supports the hypothesis that fewer aldehyde functions are present in this sample. Our experiments unambiguously confirm that **2a** has a very high tendency to form and is favoured over **2b** and **I3**, even with a ten-fold excess of DAB. Reactions in the solid state and in solution gave similar results, and no **I3** was detected. The test with free *n*-propylamine further confirmed that amine–imine interchange occurs under the applied conditions, thus making it plausible that such exchanges occur at the remaining imine functions after the hydrolytic opening of **2a** to **I1**. We postulate that when only traces of water are present, hydrolysis stops for the overwhelming majority of molecules at **I1**, which in turn cyclizes to **2b** *via* an intramolecular transimination. In addition, **I2** generated simultaneously cyclizes through intramolecular condensation to **2b**. This kinetic product is stable at elevated temperatures and in high dilution. Upon cooling or concentrating, transimination and hydrolysis of **2b** at one imine function may occur, regenerating **I1** and **I2**, respectively. Alternatively, **I2** can also recombine directly to **2a** in a concerted manner. The different possible pathways outlined in Scheme 6 highlight the complexity of the system under investigation. Although different multifunctional intermediates are involved, the conversion **2a** to **2b** (and *vice versa*) behaves in a remarkably straightforward manner and is therefore a self-sorting system.

To further elucidate the switching mechanism between **2a** and **2b**, we conducted a DFT-level theoretical investigation using four commonly employed functionals: B3LYP, B3LYP-D3, M06, and ωB97X-D. While imine hydrolysis and transimination reactions are well documented[53] and were not modelled further, the thermodynamics of the exchange process had not been characterised for this specific system. Our calculations focused on evaluating the relative free energies of **2a** and **2b**, which are expected to drive their dynamic covalent switching. However, the small anticipated energy differences ($\Delta G \approx$ 2–10 kJ mol^{-1}) present a significant challenge for computational modelling, as they are highly sensitive to the choice of functional, basis set, and solvation model. The results (Table 1) reveal that most functionals predict **2a** to be slightly more stable or nearly isoenergetic with **2b** at −25 °C, consistent with the experimental 1 : 1 equilibrium ratio. At 50 °C, **2b** is predicted to be more stable than **2a** by approximately 10 kJ mol^{-1}, although this overestimates its proportion (≥97%) compared to the experimentally observed ~1 : 3 ratio (**2a**/**2b**).

Table 1 Calculated thermodynamic parameters for the reaction **2a** → 2 **2b** at different DFT levels[a]

Functional	B3LYP	B3LYP-D3	M06	ωB97X-D
ΔG_{248} [b]	−0.2 (52)	2.3 (25)	−10.5 (99)	−0.2 (53)
ΔG_{323} [c]	−11.1 (98)	−9.1 (97)	−21.7 (100)	−12.7 (99)
ΔE [d]	32.6	41.1	26.6	40.2
$\Delta\Delta G_{corr}$ [e]	−36.2 (−47.1)	−40.0 (−51.4)	−37.4 (−46.8)	−41.8 (−54.2)
$\Delta\Delta G_{solv}$ [f]	3.4	1.3 (10.4)[g]	0.3	1.4
N–N [h]	4.161	3.843	3.790 (3.790)[i]	3.792

[a] Energy in kJ mol^{-1}. Calculations were performed using the SMD($CHCl_3$) solvation model at the DFT/def2-TZVPP//DFT/def2-SVP level of theory with B3LYP, B3LYP-D3, M06 and ωB97X-D functionals. [b] Free energy of the reaction **2** → 2 **2b** at T = 248 K. $\Delta G_T = \Delta E + \Delta\Delta G_{corr}(T) + \Delta\Delta G_{solv}$. Values in parentheses indicate the predicted equilibrium percentage of **2b**. [c] Free energy of the reaction at T = 323 K. Values in parentheses: % of **2b**. [d] Electronic energy of the reaction. [e] Change in enthalpic and entropic correction terms for the reaction at T = 248 K (values in parentheses at T = 323 K). [f] Change in solvation energy for the reaction. [g] Value for methanol. [h] N···N distance between imine groups on the same ruthenocene in **2a** (Å). Experimental values in **2a**·DCM: 4.269–4.273 Å. [i] Geometry optimised with implicit solvation.

This discrepancy underscores the inherent limitations of DFT calculations, where cumulative small errors can significantly affect the predicted energetics in finely balanced systems. Notably, the M06 functional deviates significantly from the others, predicting a much higher stability for **2a** (ΔG_{248} = −10.5 kJ mol^{-1}). The electronic energy of **2a** is approximately 30–40 kJ mol^{-1} lower than that of **2b**, indicating greater electronic stability for **2a**. Conversely, enthalpic and entropic contributions increasingly favour **2b** at elevated temperatures. Solvation effects slightly favour **2a** but are modest in chloroform. In contrast, these effects are substantially more pronounced in methanol ($\Delta\Delta G_{solv}$ = 1.3 and 10.4 kJ mol^{-1} in chloroform and methanol, respectively, at the B3LYP-D3 level), which may explain why the synthetic route shown in Scheme 1a predominantly yields **2a**. Finally, the optimised N–N distance in **2a** is accurately reproduced only when dispersion corrections are omitted, suggesting that dispersion-corrected functionals may overestimate intramolecular C–H···H–C interactions in this macrocyclic system.

Conclusions

In summary, we have demonstrated that a dimeric ruthenocene-based macrocycle **2a** can be obtained in good yields from the bifunctional 1,1′-diformylruthenocene and 1,4-diaminobutane in solution and by mechanochemical synthesis. The macrocycle exhibited a temperature- and concentration-dependent dynamic equilibrium with the corresponding ruthenocenophane **2b**. The two compounds could be switched back and forth multiple times without loss of activity. Notably, the ruthenocenophane is highly reactive and therefore could only be characterised in solution, but it could be trapped and isolated as a dication, $[H_2\text{-}\mathbf{2b}]^{2+}$. Furthermore, both the macrocycle and the ruthenocenophane were trapped as Pd-NHC adducts, yielding a large hexametallic macrocycle **3a** and trimetallic ruthenocenophane **3b**. Supported by control experiments and DFT calculations, we propose a water-catalysed transimination mechanism for the reversible transformation between both species.

Author contributions

M. R. and H. V. H. conceptualised the research. M. R. synthesised the compounds and conducted the experiments. G. F. performed the DFT calculations. All authors discussed the data and contributed to writing the manuscript.

Conflicts of interest

There are no conflicts to declare.

Data availability

The data supporting this article have been included as part of the supplementary information (SI).

Supplementary information: spectroscopic data, CIF files, computational coordinates in *xyz* format. Images of molecular structures were plotted with Olex2[56] and ellipsoids were drawn at a 50% probability level. See DOI: https://doi.org/10.1039/d6qi00665e.

CCDC 2520939 (**2a**·CH_2Cl_2), 2520940 (**2a**), 2520941 (**2a**·H_2O), 2520942 ($[H_2\text{-}\mathbf{2b}]Cl_2\cdot(H_5O_2)Cl$), 2520943 ($[H_2\text{-}\mathbf{2b}]Cl_2\cdot 2H_2O$), 2520944 ($[H_2\text{-}\mathbf{2b}]Cl_2\cdot 2H_2O$), 2520945 (**3a**), 2520946 (**3b**) contain the supplementary crystallographic data for this paper.[57a–h]

Acknowledgements

This Research/Project is supported by the National University of Singapore, Applied Materials South East Asia Pte. Ltd., and the RIE2025 Industry Alignment Fund- Industry Collaboration Project (IAF-ICP) (Award No: I2401E0029), adminstered by the Agency for Science, Technology and Research (A*STAR, Singapore).

References

1 V. Blanco, D. A. Leigh and V. Marcos, Artificial switchable catalysts, *Chem. Soc. Rev.*, 2015, **44**, 5341–5370.
2 M. Roemer, A. Gillespie, D. Jago, D. Costa-Milan, J. Alqahtani, J. Hurtado-Gallego, H. Sadeghi, C. J. Lambert,

P. R. Spackman, A. N. Sobolev, B. W. Skelton, A. Grosjean, M. Walkey, S. Kampmann, A. Vezzoli, P. V. Simpson, M. Massi, I. Planje, G. Rubio-Bollinger, N. Agraït, S. J. Higgins, S. Sangtarash, M. J. Piggott, R. J. Nichols and G. A. Koutsantonis, 2,7- and 4,9-Dialkynyldihydropyrene molecular switches: Syntheses, properties, and charge transport in single-molecule junctions, *J. Am. Chem. Soc.*, 2022, **144**, 12698–12714.

3 Q. Zhang, Y. Wang, C. Nickle, Z. Zhang, A. Leoncini, D. C. Qi, K. Sotthewes, A. Borrini, H. J. W. Zandvliet, E. Del Barco, D. Thompson and C. A. Nijhuis, Molecular switching by proton-coupled electron transport drives giant negative differential resistance, *Nat. Commun.*, 2024, **15**, 8300.

4 M. Roemer, X. Chen, Y. Li, L. Wang, X. Yu, P.-A. Cazade, C. Nickle, R. Akter, E. Del Barco, D. Thompson and C. A. Nijhuis, Supramolecular tunnelling junctions with robust high rectification based on assembly effects, *Nanoscale*, 2024, **16**, 19683–19691.

5 Y. W. Yang, Y. L. Sun and N. Song, Switchable host-guest systems on surfaces, *Acc. Chem. Res.*, 2014, **47**, 1950–1960.

6 Y. Liu, Q. Zhang, S. Crespi, S. Chen, X. K. Zhang, T. Y. Xu, C. S. Ma, S. W. Zhou, Z. T. Shi, H. Tian, B. L. Feringa and D. H. Qu, Motorized macrocycle: A photo-responsive host with switchable and stereoselective guest recognition, *Angew. Chem., Int. Ed.*, 2021, **60**, 16129–16138.

7 C. Qian, L. Feng, W. L. Teo, J. Liu, W. Zhou, D. Wang and Y. Zhao, Imine and imine-derived linkages in two-dimensional covalent organic frameworks, *Nat. Rev. Chem.*, 2022, **6**, 881–898.

8 M. E. Belowich and J. F. Stoddart, Dynamic imine chemistry, *Chem. Soc. Rev.*, 2012, **41**, 2003–2024.

9 B. Bag and J. M. Lehn, Conjugation effects in the generation of dynamic covalent libraries of bis-imines from substituted aromatic aldehyde and amine components, *Chem. – Eur. J.*, 2025, **31**, e202500152.

10 S. Gambaro, C. Talotta, P. D. Sala, A. Soriente, M. De Rosa, C. Gaeta and P. Neri, Kinetic and thermodynamic modulation of dynamic imine libraries driven by the hexameric resorcinarene capsule, *J. Am. Chem. Soc.*, 2020, **142**, 14914–14923.

11 Z. Yang, F. Esteve, C. Antheaume and J. M. Lehn, Dynamic covalent self-assembly and self-sorting processes in the formation of imine-based macrocycles and macrobicyclic cages, *Chem. Sci.*, 2023, **14**, 6631–6642.

12 Z. Yang and J. M. Lehn, Dynamic covalent self-sorting and kinetic switching processes in two cyclic orders: Macrocycles and macrobicyclic cages, *J. Am. Chem. Soc.*, 2020, **142**, 15137–15145.

13 T. Kunde, T. Pausch, P. A. Gunka, M. Krzyzanowski, A. Kasprzak and B. M. Schmidt, Fast, solvent-free synthesis of ferrocene-containing organic cages via dynamic covalent chemistry in the solid state, *Chem. Sci.*, 2022, **13**, 2877–2883.

14 A. Kasprzak and P. A. Guńka, A ferrocene-templated Pd-bearing molecular reactor, *Dalton Trans.*, 2020, **49**, 6974–6979.

15 D. E. Herbert, U. F. Mayer and I. Manners, Strained metallocenophanes and related organometallic rings containing π-hydrocarbon ligands and transition-metal centers, *Angew. Chem., Int. Ed.*, 2007, **46**, 5060–5081.

16 R. A. Musgrave, R. L. N. Hailes, V. T. Annibale and I. Manners, Role of torsional strain in the ring-opening polymerisation of low strain [n]nickelocenophanes, *Chem. Sci.*, 2019, **10**, 9841–9852.

17 R. A. Musgrave, A. D. Russell, D. W. Hayward, G. R. Whittell, P. G. Lawrence, P. J. Gates, J. C. Green and I. Manners, Main-chain metallopolymers at the static–dynamic boundary based on nickelocene, *Nat. Chem.*, 2017, **9**, 743–750.

18 S. Baljak, A. D. Russell, S. C. Binding, M. F. Haddow, D. O'Hare and I. Manners, Ring-opening polymerization of a strained [3]nickelocenophane: A route to polynickelocenes, a class of S = 1 metallopolymers, *J. Am. Chem. Soc.*, 2014, **136**, 5864–5867.

19 J. K. Pudelski and M. R. Callstrom, Structure, reactivity, and electronic properties of [4]ferrocenophanes and [4]ruthenocenophanes prepared via a novel heteroannular cyclization reaction, *Organometallics*, 1994, **13**, 3095–3109.

20 M. Roemer, D. A. Wild, A. N. Sobolev, B. W. Skelton, G. L. Nealon, M. J. Piggott and G. A. Koutsantonis, Carbon-rich trinuclear octamethylferrocenophanes, *Inorg. Chem.*, 2019, **58**, 3789–3799.

21 M. Roemer, D. A. Wild, B. W. Skelton, A. N. Sobolev, G. L. Nealon, M. J. Piggott and G. A. Koutsantonis, Control over cyclisation sequences of 1,1′-bifunctional octamethylferrocenes to ferrocenophanes, *Dalton Trans.*, 2017, **46**, 10899–10907.

22 M. Roemer, B. W. Skelton, M. J. Piggott and G. A. Koutsantonis, 1,1′-Diacetyloctamethylferrocene: An overlooked and overdue synthon leading to the facile synthesis of an octamethylferrocenophane, *Dalton Trans.*, 2016, **45**, 18817–18821.

23 K. Unverhau, G. Lübbe, B. Wibbeling, R. Fröhlich, G. Kehr and G. Erker, Frustrated Lewis pair reactions at the [3]ferrocenophane framework, *Organometallics*, 2010, **29**, 5320–5329.

24 C. Mahe, O. Blacque, G. Gasser, V. Gandon and K. Cariou, N-Metallocenyl Ynamides: Preparation, reactivity, and synthesis of ansa[3]-ferrocenylamides, *Org. Lett.*, 2023, **25**, 624–629.

25 M. Roemer and D. Lentz, Autocatalytic formation of fluorinated ferrocenophanes from 1,1′-bis(trifluorovinyl)ferrocene, *Chem. Commun.*, 2011, **47**, 7239–7241.

26 L. Zhu, J. Xu, B. Lan, X. Chen, H. Kono, H. Xu, J. Yan, W. Li, A. Yagi, Y. Yuan, K. Itami and Y. Li, Ferrocene-based conjugated macrocycles: shotgun synthesis, size-dependent properties and tunable fluorescence intensity, *Org. Chem. Front.*, 2024, **11**, 5130–5137.

27 B. Lan, J. Xu, L. Zhu, X. Chen, H. Kono, P. Wang, X. Zuo, J. Yan, A. Yagi, Y. Zheng, S. Chen, Y. Yuan, K. Itami and Y. Li, Side-chain type ferrocene macrocycles, *Precis. Chem.*, 2024, **2**, 143–150.

28 L. E. Wilson, C. Hassenruck, R. F. Winter, A. J. P. White, T. Albrecht and N. J. Long, Ferrocene- and biferrocene-con-

taining macrocycles towards single-molecule electronics, *Angew. Chem., Int. Ed.*, 2017, **56**, 6838–6842.
29 M. S. Inkpen, S. Scheerer, M. Linseis, A. J. White, R. F. Winter, T. Albrecht and N. J. Long, Oligomeric ferrocene rings, *Nat. Chem.*, 2016, **8**, 825–830.
30 S. Akabori, H. Munegumi, S. Sato and M. Sato, Syntheses of polythia[*n*]ruthenocenophanes, *J. Organomet. Chem.*, 1984, **272**, C54–C56.
31 P. D. Beer, A. D. Keefe, H. Sikanyika, C. Blackburn and J. F. McAleer, Metallocene bis(aza-crown ether) ligands and related compounds. Their syntheses, co-ordination chemistry, and electrochemical properties, *J. Chem. Soc., Dalton Trans.*, 1990, 3289–3294.
32 I. Grocka, L. Latos-Grazynski and M. Stepien, Ruthenocenoporphyrinoids: Conformation determines macrocyclic π conjugation transmitted across a d-electron metallocene, *Angew. Chem., Int. Ed.*, 2013, **52**, 1044–1048.
33 P. D. Beer, Z. Chen, M. G. B. Drew, A. O. M. Johnsona, D. K. Smith and P. Spencer, Transition metal cation and phosphate anion electrochemical recognition in water by new polyaza ferrocene macrocyclic ligands, *Inorg. Chim. Acta*, 1996, **246**, 143–150.
34 E. Bullita, U. Casellato, F. Ossola, P. Tomasin, P. A. Vigato and U. Russo, Synthesis, X-ray structural determination and Mössbauer characterization of Schiff bases bearing ferrocene groups, their reduced analogues and related complexes, *Inorg. Chim. Acta*, 1999, **287**, 117–133.
35 Y. Lin, H. Jung, C. A. Bulman, J. Ng, R. Vinck, C. O'Beirne, S. Zhong, M. S. Moser, N. Tricoche, R. Peguero, R. W. Li, J. F. Urban Jr., P. L. Pape, F. Pagniez, M. Moretto, T. Weil, S. Lustigman, K. Cariou, M. Mitreva, J. A. Sakanari and G. Gasser, Discovery of new broad-spectrum anti-infectives for eukaryotic pathogens using bioorganometallic chemistry, *J. Med. Chem.*, 2023, **66**, 15867–15882.
36 A. Caballero, A. Espinosa, A. Tárraga and P. Molina, Synthesis, electrochemical, and optical properties of linear homo- and heterometallocene triads, *J. Org. Chem.*, 2007, **72**, 6924–6937.
37 A. Caballero, R. García, A. Espinosa, A. Tárraga and P. Molina, Multifunctional ferrocene–ruthenocene dyads linked by single or double aza-containing bridges displaying metal–metal interactions and cation recognition properties, *J. Org. Chem.*, 2007, **72**, 1161–1173.
38 T. E. Shaw, J. Arami, J.-F. Ayme, J.-M. Lehn and T. Jurca, Dynamic mechanochemistry: Accelerated self-sorting of two imine-based metal complexes under solvent-free mechanochemical conditions, *RSC Mechanochem.*, 2024, **1**, 33–37.
39 P. D. Beer, Z. Chen, M. G. B. Drew, J. Kingston, M. Ogden and P. Spencer, New polyaza and polyammonium ferrocene macrocyclic ligands that complex and electrochemically recognise transition metal cations and phosphate anions in water, *J. Chem. Soc. D*, 1993, 1046–1048.
40 J. K. Pudelski and M. R. Callstrom, A highly efficient route to ferrocene derivatives containing four-carbon heteroannular bridges via a novel cyclization reaction, *Organometallics*, 1992, **11**, 2757–2759.
41 M. Roemer, Y. K. Kang, Y. K. Chung and D. Lentz, Ferrocenes with perfluorinated side chains and ferrocenophanes with fluorinated handles, *Chem. – Eur. J.*, 2012, **18**, 3371–3389.
42 G. Zundel and H. Metzger, Energiebänder der tunnelnden Überschuß-Protonen in flüssigen Säuren. Eine IR-spektroskopische Untersuchung der Natur der Gruppierungen $H_5O_2^+$, *Z. Phys. Chem.*, 1968, **58**, 225–245.
43 J. L. Fulton and M. Balasubramanian, Structure of hydronium (H_3O^+)/chloride (Cl) contact ion pairs in aqueous hydrochloric acid solution: A Zundel-like local configuration, *J. Am. Chem. Soc.*, 2010, **132**, 12597–12604.
44 Y. Tian, J. Hong, D. Cao, S. You, Y. Song, B. Cheng, Z. Wang, D. Guan, X. Liu, Z. Zhao, X.-Z. Li, L.-M. Xu, J. Guo, J. Chen, E.-G. Wang and Y. Jiang, Visualizing Eigen/Zundel cations and their interconversion in monolayer water on metal surfaces, *Science*, 2022, **377**, 315–319.
45 K. Molčanov, J. Stare, M. V. Vener, B. Kojić-Prodić, G. Mali, J. Grdadolnik and V. Mohaček-Gročev, Nitranilic acid hexahydrate, a novel benchmark system of the Zundel cation in an intrinsically asymmetric environment: Spectroscopic features and hydrogen bond dynamics characterised by experimental and theoretical methods, *Phys. Chem. Chem. Phys.*, 2014, **16**, 998–1007.
46 E. K. Andersen, The crystal and molecular structure of hydroxyquinones and salts of hydroxyquinones. V. Hydronium nitranilate, nitranilic acid hexahydrate, *Acta Cryst.*, 1967, **22**, 204–208.
47 K. Molčanov, C. Jelsch, E. Wenger, J. Stare, A. Ø. Madsen and B. Kojić-Prodić, Experimental evidence of a 3-centre, 2-electron covalent bond character of the central O–H–O fragment on the Zundel cation in crystals of Zundel nitranilate tetrahydrate, *CrystEngComm*, 2017, **19**, 3898–3901.
48 A. A. Hoser, Ł. Dobrzycki, M. J. Gutmann and K. Woźniak, Charge densities of two polymorphs of hydrated 1,8-bis(dimethylamino)naphthalene hydrochloride – similarities and differences, *Cryst. Growth Des.*, 2010, **10**, 5092–5104.
49 L. Dobrzycki, M. Chruszcz, W. Minor and K. Woźniak, Stacks of $DMANH^+$– scaffolding for ribbon shaped Cl^- bridged oxonium ions, *CrystEngComm*, 2007, **9**, 152–157.
50 H. V. Huynh, Y. Han, J. H. H. Ho and G. K. Tan, Palladium (II) complexes of a sterically bulky, benzannulated N-heterocyclic carbene with unusual intramolecular C–H···Pd and ccarbene···Br interactions and their catalytic activities, *Organometallics*, 2006, **25**, 3267–3274.
51 H. V. Huynh, Recent applications of the Huynh Electronic Parameter (HEP), *Chem. Lett.*, 2021, **50**, 1831–1841.
52 Y. Han, H. V. Huynh and G. K. Tan, Syntheses and characterizations of Pd(II) complexes incorporating a *N*-heterocyclic carbene and aromatic *N*-heterocycles, *Organometallics*, 2007, **26**, 6447–6452.
53 M. Ciaccia, R. Cacciapaglia, P. Mencarelli, L. Mandolini and S. D. Stefano, Fast transimination in organic solvents in the absence of proton and metal catalysts. A key to imine metathesis catalyzed by primary amines under mild conditions, *Chem. Sci.*, 2013, **4**, 2253–2261.

54 M. Ciaccia, S. Pilati, R. Cacciapaglia, L. Mandolini and S. D. Stefano, Effective catalysis of imine metathesis by means of fast transiminations between aromatic-aromatic or aromatic-aliphatic amines, *Org. Biomol. Chem.*, 2014, **12**, 3282–3287.

55 R. Sanders and U. T. Mueller-Westerhoff, The lithiation of ferrocene and ruthenocene: a retraction and an improvement, *J. Organomet. Chem.*, 1996, **512**, 219–224.

56 O. V. Dolomanov, L. J. Bourhis, R. J. Gildea, J. A. K. Howard and H. Puschmann, OLEX2: A complete structure solution, refinement and analysis program, *J. Appl. Crystallogr.*, 2009, **42**, 339–341.

57 (*a*) CCDC 2520939: Experimental Crystal Structure Determination, 2026, DOI: **10.5517/ccdc.csd.cc2qm7m7**; (*b*) CCDC 2520940: Experimental Crystal Structure Determination, 2026, DOI: **10.5517/ccdc.csd.cc2qm7n8**; (*c*) CCDC 2520941: Experimental Crystal Structure Determination, 2026, DOI: **10.5517/ccdc.csd.cc2qm7p9**; (*d*) CCDC 2520942: Experimental Crystal Structure Determination, 2026, DOI: **10.5517/ccdc.csd.cc2qm7qb**; (*e*) CCDC 2520943: Experimental Crystal Structure Determination, 2026, DOI: **10.5517/ccdc.csd.cc2qm7rc**; (*f*) CCDC 2520944: Experimental Crystal Structure Determination, 2026, DOI: **10.5517/ccdc.csd.cc2qm7sd**; (*g*) CCDC 2520945: Experimental Crystal Structure Determination, 2026, DOI: **10.5517/ccdc.csd.cc2qm7tf**; (*h*) CCDC 2520946: Experimental Crystal Structure Determination, 2026, DOI: **10.5517/ccdc.csd.cc2qm7vg**.